Layered LaCuOSe: A Promising Anisotropic Thermoelectric Material

Ning Wang, Menglu Li, Haiyan Xiao,* Xiaotao Zu,† and Liang Qiao‡

School of Physics, University of Electronic Science and Technology of China, Chengdu 610054, China

Thermoelectric (TE) materials can convert temperature diffferences into electricity directly and reversibly without air pollution, which provides a viable route for alleviating global warming and the energy crisis. Here, we use first-principles calculations combined with semiclassical Boltzmann transport theory to assess the potential of layered LaCuOSe for TE applications. Originating from the layered crystal structure, the electronic and thermal transport properties (i.e., Seebeck coefficient, electrical conductivity, and thermal conductivity) are highly anisotropic between the in-plane and out-of-plane directions. The optimal figure of merit of 2.71 is achieved along the out-of-plane direction for electron doping at 900 K. Such excellent TE properties can be attributed to desired La-Se interlayer interaction between adjacent layers and relatively strong coupling between acoustic phonons and optical phonons, resulting in simultaneous enhancement of the electrical conductivity and suppression of the lattice thermal conductivity. This study provides an effective route to improve the TE performance of layered LaCuOSe by utilizing the anisotropic character of transport properties and offers implications in promoting related experimental investigations.

I. INTRODUCTION

Ever-increasingly serious energy shortage and the greenhouse effect have become global issues, which strongly demand renewable and clean energy resources [1–6]. In recent years, thermoelectric (TE) materials, which are capable of directly and reversibly converting temperature differences into electricity via the Seebeck and Peltier effect, have been considered as one highly possible solution [7–11]. The efficiency of TE materials can be measured by the figure of merit, $ZT = S^2 \sigma T / \kappa$, in which S, σ, T, and κ are the Seebeck coefficient, electrical conductivity, temperature, and thermal conductivity, respectively [12]. An excellent TE material should exhibit a large Seebeck coefficient, a high electrical conductivity, and low thermal conductivity. Nevertheless, due to strong inherent coupling of these coefficients, it is not easy to increase the power factor, PF ($S^2\sigma$), and reduce the thermal conductivity simultaneously [13]. Thus, to improve the conversion efficiency of TE materials, several strategies have been developed, e.g., grain boundary engineering [14,15], interface engineering [16,17], band-structure engineering [18,19], nanostructure engineering [20,21], and strain engineering [22,23]. Apart from optimizing existing TE materials, the exploration of TE materials is another important way to improve TE conversion efficiency, i.e., finding materials with excellent TE performance in existing materials and predicting alternative TE materials [11,24]. The specific methods for materials discovery include experimental research [25–28] and theoretical prediction (such as first-principles calculations [11,29], high-throughput computations [30–32]). For example, first-principles calculations carried out by Tao *et al.* [11] reveal that the new two-dimensional (2D) material InP$_3$, which has outstanding optical character and great potential in photovoltaic solar cells, is also an excellent TE material.

Layered materials attract wide attention due to their intrinsic ultralow lattice thermal conductivities and large Seebeck coefficients [29,33]. These properties mainly depend on the coupling between adjacent layers, which can be either weak van der Waals (vdW) interactions [29] or sizable quasi-covalent bonding [34–36]. Generally, the interface interactions between adjacent layers cause large phonon anharmonicity, leading to dissipative phonon transport and ultralow lattice thermal conductivity. Such characteristics enable layered materials to show potential as TE materials. However, because of the absence of effective bonding between adjacent layers in conventional vdW layered materials, their electrical conductivities are usually low [29]. Therefore, if suitable layered materials with relatively strong interlayer coupling, and thus, high electrical conductivity can be identified, then these materials may exhibit large *ZT* values.

*hyxiao@uestc.edu.cn
†xtzu@uestc.edu.cn
‡liang.qiao@uestc.edu.cn

As a classic *p*-type layered oxychalcogenide semiconductor, LaCuOSe exhibits interesting photoelectric, magnetic, and electronic transport properties, which have been the previous focus for this material [37–39]. On the other hand, the natural layered structure of LaCuOSe combined with excellent intrinsic electrical properties suggest its potential for TE applications. From the crystal structure perspective, the $(Cu_2Se_2)^{2-}$ layers in LaCuOSe can be considered as the two-dimensional sublattice of the traditional TE material Cu_2Se [see Figs. 1(a) and 1(b)] [40]. Due to the carrier confinement effect in the $(Cu_2Se_2)^{2-}$ layers, the Seebeck coefficient of LaCuOSe is expected to be higher than that of bulk Cu_2Se [41]. From the bonding perspective, the large difference among La—Se, La—O, and Cu—Se bonds in layered LaCuOSe leads to large phonon anharmonicity, and thus, to low lattice thermal conductivity. Very importantly, this layered crystal exhibits high electrical conductivity, and the electrical conductivity can be controlled by element doping [42]. Recently, Yasukawa *et al*. took the first step to experimentally study the possibility of applying this material toward TE applications by measuring the thermoelectric properties for both pristine and doped LaCuOSe [43]. They find that Sr doping can significantly increase the electrical conductivity, thus leading to an enhancement of the power factor, while its Seebeck coefficient is still small

and there are no reliable reports on the thermal conductivity or *ZT* value. On the other hand, Hidenori *et al*. report that the carrier mobility and effective mass of LaCuOSe are of anisotropic character, originating from the layered crystal structure [39]. Saha and Dutta find that the thermal conductivity of LaCuOSe exhibits strong anisotropy [44]. As a result, it is expected that the thermoelectric properties of LaCuOSe are anisotropic, which might provide a possibility to obtain a high figure of merit (*ZT*) along a certain direction. Unfortunately, systemic studies on the TE performance of LaCuOSe, especially the direction-dependent thermal-electric properties, are not yet reported.

Here, the electronic and thermal transport properties of LaCuOSe are systematically studied using first-principles methods combined with semiclassical Boltzmann transport theory. The effects of La-Se interaction between adjacent layers and anharmonic interaction of phonons on the TE performance of LaCuOSe are investigated. The optimal *ZT* value of LaCuOSe is strongly direction dependent, which is as high as 2.71 at 900 K along the *c* axis direction and 0.26 along the *a* axis direction. Therefore, LaCuOSe has great potential in the application of highly efficient TE materials. This study demonstrates that layered LaCuOSe can achieve high thermal-electric performance by utilizing the anisotropic character of transport properties, which is
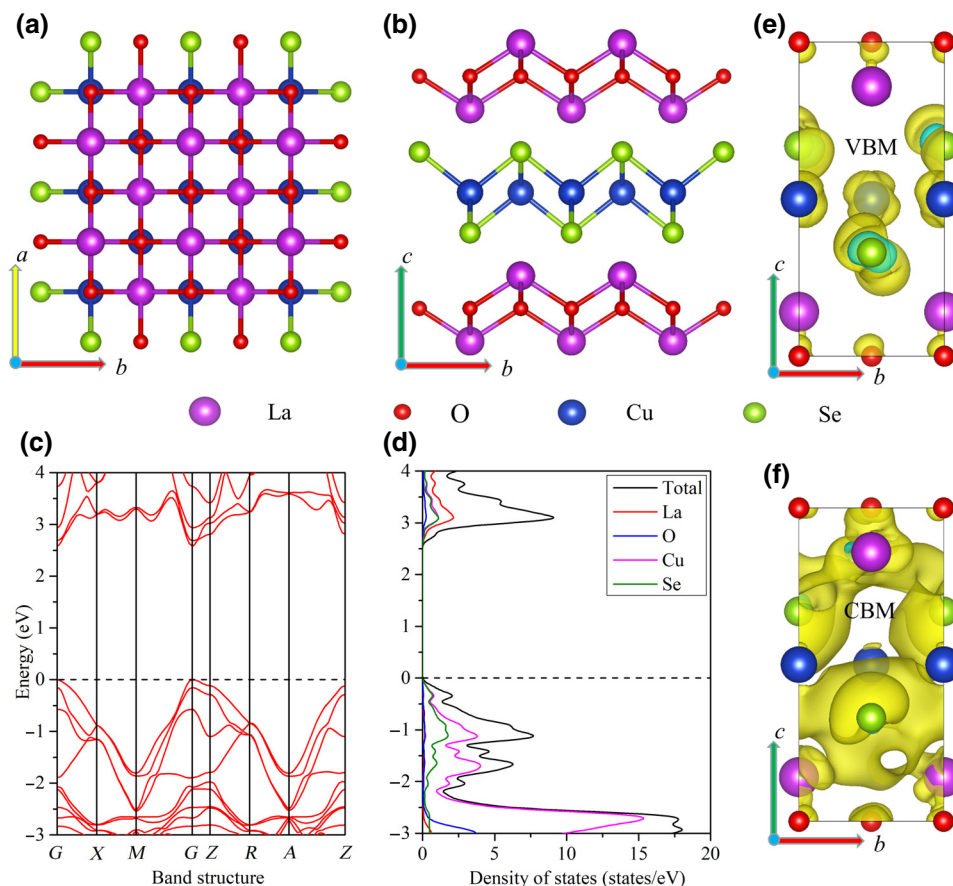

FIG. 1. Top view (a) and front view (b) of the crystal structure of LaCuOSe. The calculated band structure (c) and total and partial density of states (d) for LaCuOSe. The calculated band-decomposed charge density of valence bands (e) and conduction bands (f) near the Fermi level at *G* point for LaCuOSe.

of important significance for promoting related theoretical and experimental investigations.

II. COMPUTATIONAL DETAILS

Our first-principles calculations are performed by using density functional theory (DFT), as implemented in the Vienna *ab initio* Simulation Package (VASP) code [45–47]. The exchange-correlation effects are treated by the generalized gradient approximation (GGA) [48,49] in the Perdew-Burke-Ernzerhof (PBE) parametrization [50]. To obtain accurate electronic structure and transport coefficients, the Heyd-Scuseria-Ernzerhof hybrid functional (HSE06) [51] is adopted to describe the exchange-correlation energy, and the effect of spin-orbit coupling (SOC) is considered. The plane-wave kinetic energy cutoff is set at 400 eV. We perform a series of test calculations to determine the k-point sampling for evaluating the transport coefficients. Figure 2 shows the ratio of electrical conductivity to relaxation time (σ/τ) and Seebeck coefficients, S, along the a and c axes for n- and p-type LaCuOSe obtained by employing $6 \times 6 \times 3$, $8 \times 8 \times 4$, $10 \times 10 \times 5$, and $12 \times 12 \times 6$ k-point samplings. It is shown that the $12 \times 12 \times 6$ Monkhorst-Pack k-mesh can provide converged results. This k-point sampling, thus, is employed in our study to evaluate the transport coefficients. The convergence criteria for energy and force are 10^{-4} and 10^{-5} eV/Å, respectively. The electronic transport coefficients of both n- and p-type LaCuOSe are obtained by semiclassical Boltzmann theory within the relaxation-time approximation (RTA) in the BoltzTraP2 code [52]. The relaxation time (τ) is calculated by the deformation potential (DP) theory [53]. The second- and third-order interatomic force constants (IFCs), as inputs of the Phonopy package [54] and ShengBTE code [55] to calculate the phonon structure and lattice thermal conductivity, respectively, are obtained by using $4 \times 4 \times 1$ and $3 \times 3 \times 1$ supercells, which contain 128 and 72 atoms, respectively. The crystal structure is plotted using VESTA software [56].

III. RESULTS AND DISCUSSIONS

A. Crystal structure and electronic structure of LaCuOSe

LaCuOSe crystallizes in a Zu-Si-Cu-As-type structure with the $P4/nmm$ (No. 129) space group [57]. The antifluorite layers $(La_2O_2)^{2+}$ and fluoritelike layers $(Cu_2Se_2)^{2-}$ are stacked perpendicularly along the c axis in the tetragonal unit cell, as shown in Figs. 1(a) and 1(b). Our
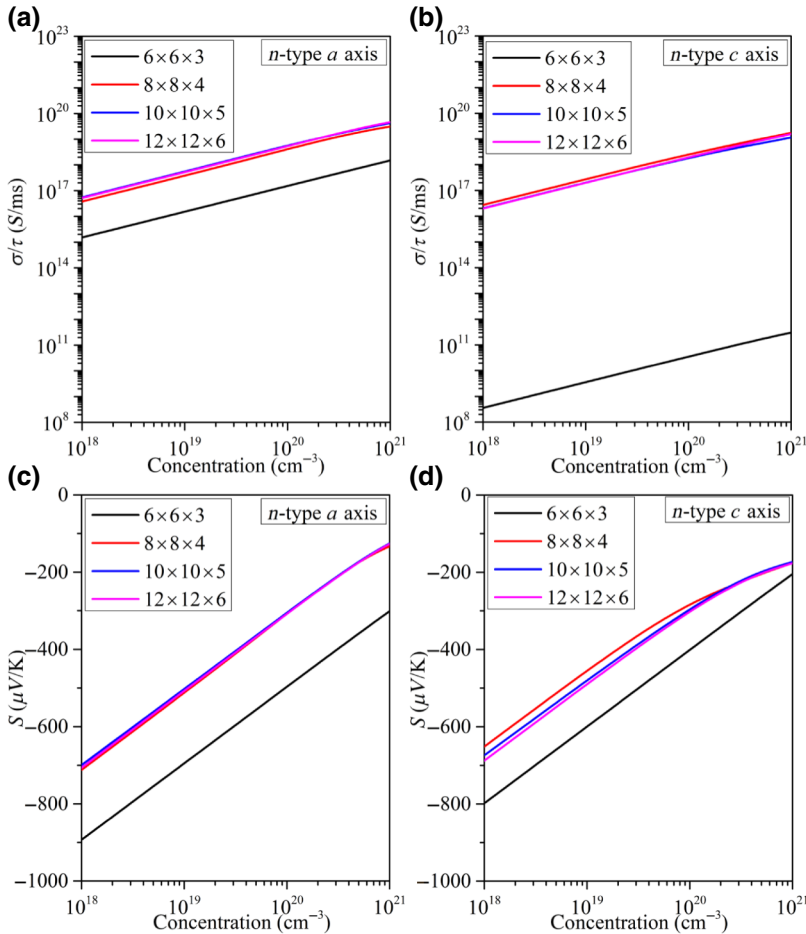

FIG. 2.   Seebeck coefficient, S [(a),(b)], and ratio of electrical conductivity to relaxation time, σ/τ [(c),(d)], along the a and c axes as a function of carrier concentration for n-type LaCuOSe at 900 K obtained by different K-point sampling in the Brillouin zone.

TABLE I. The calculated equilibrium lattice constants, interlayer spacing (d), and band gaps (E_g) for LaCuOSe and other TE materials. The obtainable experimental and theoretical values are also listed.

		a (Å)	b (Å)	c (Å)	d (Å)	E_g (eV)
LaCuOSe	Our calc	4.06	4.06	8.77	1.66	2.59
	Other calc [44]	4.02	4.02	8.65	1.64	1.4
	Expt. [57]	4.07	4.07	8.80	−	2.8
LaCuOS	Other calc [81]	3.99	3.99	8.52	1.61	1.67
	Expt. [57]	3.99	3.99	8.52	−	3.2
LaCuOTe	Other calc [81]	4.18	4.18	9.34	1.83	1.2
	Expt. [57]	4.18	4.18	9.34	−	2.3
BiCuOS	Other calc [82]	3.88	3.88	8.60	1.59	0.67
	Expt. [83]	3.87	3.87	8.56	−	1.1
BiCuOSe	Other calc [82]	3.94	3.94	9.02	1.67	0.47
	Expt. [83]	3.93	3.93	8.93		0.8
BiCuOTe	Other calc [82]	4.04	4.04	9.93	1.84	0.21
	Expt. [83]	4.04	4.04	9.52	−	0.4
PtS$_2$	Other calc [35]	3.58	3.58	6.25	2.54	0.48
PtSe$_2$	Other calc [36]	3.76	3.76	6.12	3.27	−
GeAs$_2$	Other calc [29]	10.15	14.84	3.71	1.02	0.96
SnSe	Other calc [84]	11.79	4.22	4.55	3.01	0.6
SnS$_2$	Other calc [69]	3.70	3.70	6.98	3.60	2.04
SnSe$_2$	Other calc [69]	3.87	3.87	6.91	3.58	1.09

optimized equilibrium lattice constants are $a = 4.06$ Å and $c = 8.77$ Å, which are consistent with the experimental values of $a = 4.07$ Å and $c = 8.80$ Å [57] and other calculation results of $a = 4.02$ Å and $c = 8.65$ Å [44] (see Table I). The nearest atoms between adjacent layers are La and Se atoms, and the vertical interlayer spacing of 1.66 Å between the adjacent layers of LaCuOSe is smaller than that in many typical layered materials. For example, the interlayer spacings are 2.54 Å in platinum disulfide (PtS$_2$) [35] and 3.27 Å in black phosphorus (PtSe$_2$) [36]. Table I also shows the interlayer spacing of some typical TE materials for comparison. It is known that the vertical interlayer spacing of layered material is critical for determining the electronic structure, and thus, related electrical or thermoelectric properties. For example, an ultrasmall interlayer spacing of near 1 Å for layered GeAs$_2$ is shown to significantly increase the out-of-plane electrical conductivity [29]. Thus, it is expected that such a short vertical interlayer spacing in LaCuOSe may also provide desired channels for electron transport between the $(La_2O_2)^{2+}$ and $(Cu_2Se_2)^{2-}$ layers.

The band structure and density of state distribution for LaCuOSe are plotted in Figs. 1(c) and 1(d), respectively. It is shown that both the conduction band minimum (CBM) and valence band maximum (VBM) are positioned at the G point, indicating that the band gap is of direct character. Additionally, the conduction band (valence band) around the Fermi level is mainly contributed to by La atoms (Cu and Se atoms), in analogy to other La-based thermoelectric perovskites with similar crystal structures and lattice parameters [58–61]. The calculated band gap of 2.59 eV is in good agreement with the experimental value of 2.8 eV

[57]. Since the HSE06 functional and SOC effects are considered in this calculation, our result is larger than that of the standard DFT and GGA result of 1.4 eV [44] (see Table I).

B. Relaxation time and electron-transport properties of LaCuOSe

Based on the optimized structure, the thermoelectric properties of LaCuOSe in the temperature range of 300–900 K are investigated. Experimentally, it has been reported that LaCuOSe can exist stably at about 673 K, and this material can be sintered at a temperature higher than 1200 K [43,62]. In the literature, the phase stability of LaCuOSe between 600 and 900 K has not been reported thus far, while its analogs, i.e., LaCuOSe [63] and BiCuOSe [64], have been reported to exist stably at 900 K. In this study, an *ab initio* molecular dynamics (AIMD) method is employed to investigate the phase stability of LaCuOSe under different temperatures. The calculations are performed using a canonical ensemble (NVT) with a Nóse-Hoover heat bath scheme [65]. Figure 3(a) shows the evolution of free energy of LaCuOSe with time at temperatures of 300, 600, and 900 K. The simulation time of 4 ps is used to ensure that the system reaches equilibrium under different temperatures. The equilibrium geometrical structures of LaCuOSe at temperatures of 300, 600, and 900 K are illustrated in Figs. 3(b)–3(d), respectively. It is shown that LaCuOSe remains crystalline between 300 and 900 K.

According to the relaxation-time approximation, the energy-dependent electrical conductivity can be calculated
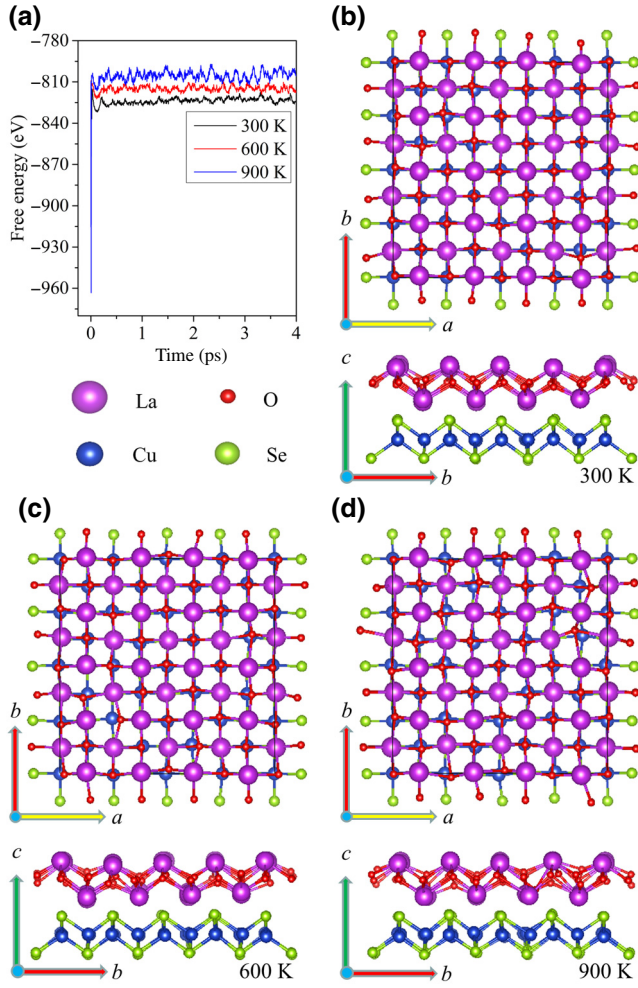
FIG. 3. (a) Free energy fluctuations with respect to time in AIMD simulations at different temperatures for LaCuOSe. (b)–(d) Equilibrium structures of LaCuOSe obtained by AIMD simulations at 300–900 K.

VBM. Considering the temperature evolution, the values of $k_B T$ are 0.026 eV at 300 and 0.078 eV for 900 K, i.e., the distribution range of carriers is expected to be increased by thermal excitation as the temperature rises. The energy difference between the lowest two conduction bands (highest two valence bands) for LaCuOSe at the G point is about 0.1 (0.15) eV, which is close to the value of 0.078 eV for $k_B T$ at 900 K, and thus, the conduction band next to CBM (CB1) and the valence band next to VBM (VB1) may also affect the electrical conductivity of LaCuOSe at high temperatures. We further calculate the probabilities of carrier occupation (f^0) for CB1, CBM, VB1, and VBM, and we find that the ratios of f^0 for CB1 to that for CBM, i.e., $f^0_{(CB1)}/f^0_{(CBM)}$, are 2.87% at 300 K and 30.9% at 900 K. Similarly, the ratios of f^0 for VB1 to that for VBM, i.e., $f^0_{(VB1)}/f^0_{(VBM)}$, are 0.27% at 300 K and 13.9% at 900 K. The results indicate that the electrical conductivity mechanism of LaCuOSe is significantly affected by temperature. At low temperatures, conductivity is mostly contributed to by the CBM and VBM, while, at high temperatures, both CB1 and VB1 participate in conduction. Here, we note that, although more electrons (bands) are involved, the overall macroscopic conductivity is still limited by phonon scattering at high temperatures [see Figs. 4(c) and 4(d)]. Additionally, for n- or p-type doped LaCuOSe, the doped carriers will be distributed on higher (lower) energy levels, and thus, enhance the electron-transport performance.

Based on the Eq. (1), the relaxation time, τ (the average time between two consecutive scattering events), is required for the calculation of the electrical conductivity, σ [52]. According to the single parabolic band (SPB) model [66], the energy-dependent relaxation time can be defined as $\tau(E) = \tau_0 E^r$, where the scatting mechanism parameter, r, is set as $-1/2$. The acoustic phonon scattering-limited relaxation time, τ_0, is given by the DP theory [53]

$$\tau_0 = \frac{h^4 C_{ii}}{8\pi^3 k_B T (2m^*)^{3/2} E_1^2}, \quad (2)$$

where h, C_{ii}, k_B, m^*, and E_1 are the Planck constant, elastic constant, Boltzmann constant, effective mass, and DP constant, respectively. The calculated values of m^*, E_1, and C_{ii} are listed in Table II. The carrier-concentration-dependent relaxation time for both p- and n-type LaCuOSe at 300, 600, and 900 K are shown in Figs. 4(a) and 4(b), respectively. First, the relaxation time is dependent on carrier types, i.e., the hole relaxation time is smaller than the electron relaxation time at the same temperature due to the lower chemical potential with hole doping. Second, the relaxation time is also dependent on crystal orientations, mainly due to different elastic constants and DP constants, as well as the coupling between in-plane and out-of-plane directions. For p-type LaCuOSe, the hole relaxation time along the a axis (solid lines) direction is smaller than that

as [29]

$$\sigma = \frac{e^2}{\Omega} \int \tau(k) v(k) v(k) \left[-\frac{\partial f^0}{\partial E} \right] dk, \quad (1)$$

where e, Ω, $\tau(k)$, $v(k)$, and f^0 are the electron charge, volume of the unit cell, relaxation time, group velocity, and Fermi-Dirac distribution function, respectively. f^0 is the probability of a quantum state with energy E being occupied by an electron. For classic metals, the values of $\partial f^0/\partial E$ are typically concentrated near the Fermi level in the energy range of $E_f - (k_B T/2)$ to $E_f + (k_B T/2)$. However, for classic semiconductors, due to the existence of the forbidden energy gap, the effective density of states for carriers only becomes nonzero starting from band edges, e.g., the VBM and CBM. Thus, generally only carriers near the CBM and VBM contribute to the electrical conductivities of semiconductors, and most of these carriers are essentially distributed in the range of $k_B T$ near the CBM and
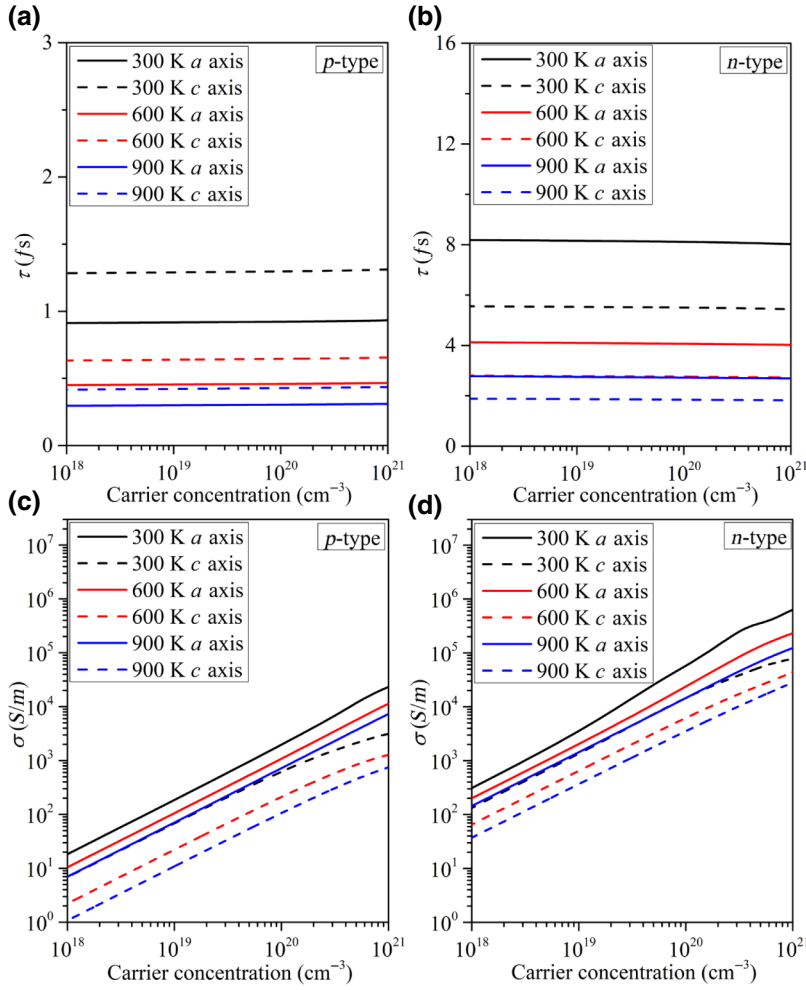
FIG. 4. Calculated relaxation time, τ [(a),(b)], and electrical conductivity, σ [(c),(d)], as a function of carrier concentration for LaCuOSe.

along the c axis (dashed lines) direction under each considered temperature [Fig. 4(a)]. However, n-type LaCuOSe shows the opposite trend, i.e., the electron relaxation time is higher along the a axis [Fig. 4(b)]. Third, relaxation time decreases as temperature rises, i.e., the relaxation times for p- and n-type LaCuOSe vary over a large range from 1.6 to 0.3 f s and 8.2 to 1.8 f s at temperatures of 300–900 K, due to more frequent scattering of carriers at higher temperature [29,67]. Frequent scattering suppresses the transport of carriers and leads to low electrical conductivity. Thus, the large reduction in relaxation time suggests that the electrical conductivity of LaCuOSe decreases markedly as the temperature rises. A similar strong dependence of relaxation time on temperature is also found in other anisotropic layered materials, e.g., the relaxation times are 13–2 f s for GeAs$_2$ [29] and 32–4 f s for GeSe [67] at 300–800 K.

Based on the obtained relaxation time, anisotropic electrical conductivity (σ) of LaCuOSe is obtained and the results are plotted in Figs. 4(c) and 4(d). In all cases, the electrical conductivities of both p- and n-type LaCuOSe increase as the carrier concentration rises. Regardless of carrier types, σ along the a axis (solid lines) is always

higher than that along the c axis (dashed lines) at each temperature, e.g., at room temperature, σ along the a axis is about three times higher than that along the c axis. This difference is even more significant at higher temperature, for example, at 900 K, σ along the a axis is nearly one order of magnitude higher than that along the c axis (see values in Table III). This electrical conductivity anisotropy is due to the relatively weaker interactions between layers along the c axis, which is consistent with previously reported characteristics of layered materials [68,69]. Moreover, at a given orientation and temperature, the electrical conductivity

TABLE II. The calculated DP constant E_1, elastic constant C_{ii}, and effective mass m^* for LaCuOSe. The m_e is the electronic mass.

	Carrier type	E_1 (eV)	C_{ii} (GPa)	m^* (m_e)
a axis	Electron	-15.56	92.0	0.34
	Hole	-8.23	92.0	2.47
c axis	Electron	-13.57	61.2	0.37
	Hole	-9.25	61.2	1.84

TABLE III.   The calculated electrical conductivity σ and Seebeck coefficient S of LaCuOSe for carrier concentrations of 1×10^{18} and 1×10^{21} cm^{-3}.

		p-type				n-type			
		1×10^{18} cm^{-3}		1×10^{21} cm^{-3}		1×10^{18} cm^{-3}		1×10^{21} cm^{-3}	
		a axis	c axis	a axis	c axis	a axis	c axis	a axis	c axis
σ (S/m)	300 K	18.8	6.9	22 842.4	3072.1	308.6	129.9	640 561.1	76 740.3
	600 K	10.2	2.2	11 298.5	1255.2	196.3	64.2	225 083.2	43 477.1
	900 K	6.9	1.1	7222.2	725.6	141.5	36.6	121 878.2	27 791.3
S (μV/K)	300 K	630.0	560.0	60.5	23.6	−643.7	−484.6	−44.6	−53.7
	600 K	706.3	629.5	117.3	58.4	−671.5	−590.9	−86.4	−126.4
	900 K	743.2	676.6	153.1	111.2	−707.5	−687.6	−126.3	−178.9

of n-type LaCuOSe is larger than that of p-type LaCuOSe. For example, at room temperature, n-type LaCuOSe shows typically 16–25 times higher electrical conductivity than that of p-type doping (depending on orientation and carrier concentration), while, at a higher temperature of 900 K, this difference is increased to 40 times for c orientation (see Table III). Apparently, the higher electrical conductivity for the n-type case is consistent with its longer relaxation time. Yet, according to Eq. (1), τ is not the only parameter to determine σ. Therefore, to

explore the origin of different transport behaviors of electrons and holes, the band-decomposed charge densities near the Fermi level are also plotted, as shown in Figs. 1(e) and 1(f). In our calculation, the isosurface level is set at a value of 0.0005. At the VBM, the charge densities of atoms show strong localization and no conducive pathways are generated between atoms at this isosurface value, leading to weak charge transfer and low electrical conductivity for p-type LaCuOSe [Fig. 1(e)]. In contrast, at the CBM, the electron density distribution is much more delocalized
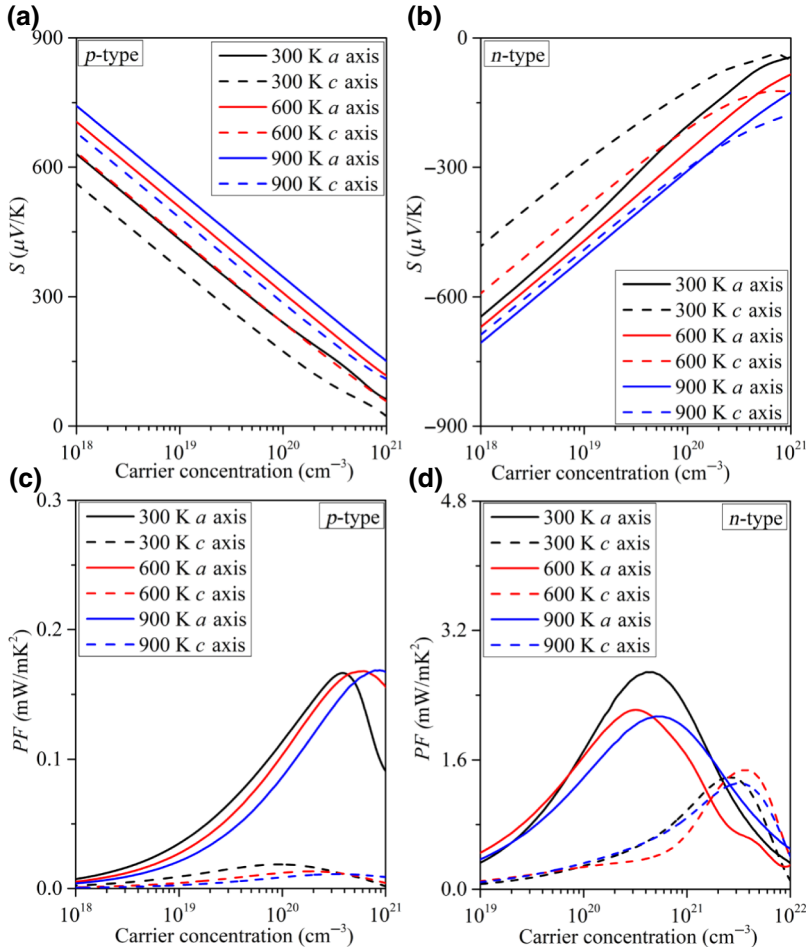

FIG. 5. Calculated Seebeck coefficient, S [(a),(b)], and power factor, PF [(c),(d)], as a function of carrier concentration for LaCuOSe.
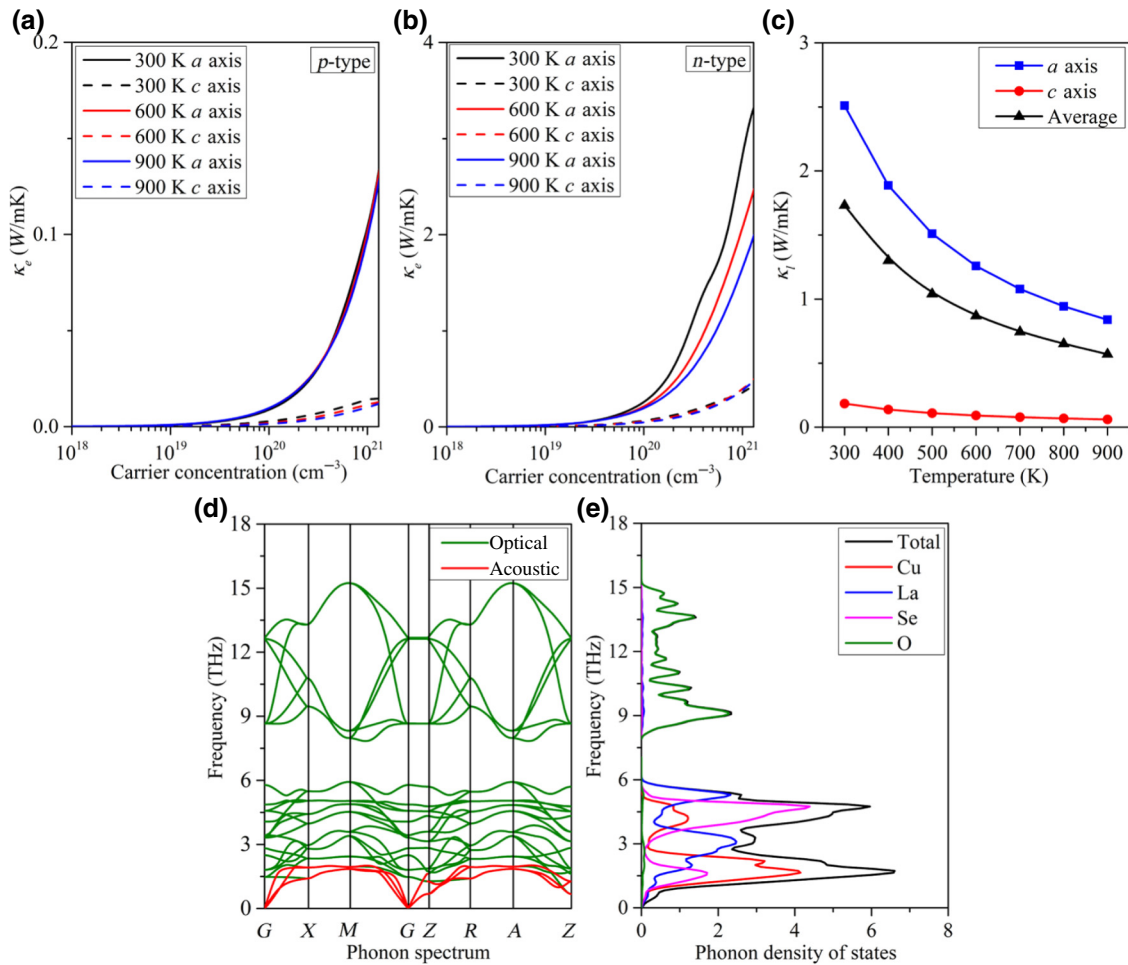
FIG. 6. Calculated electronic thermal conductivity, κ_e, for p- (a) and n-type (b) LaCuOSe as a function of carrier concentration. (c) Calculated lattice thermal conductivity, κ_l, as a function of temperature. The calculated phonon dispersion (d) and phonon total and partial density of states (e) for LaCuOSe.

over the La and Se atoms, resulting in La-Se interaction and conduction-channel formation for electrons between the $(La_2O_2)^{2+}$ and $(Cu_2Se_2)^{2-}$ layers along the out-of-plane direction. Moreover, the electron conduction pathway is also found within the in-plane $(Cu_2Se_2)^{2-}$ layers [Fig. 1(f)]. The formation of multiple electron-conduction channels accounts for the observed high conductivity of n-type LaCuOSe [70].

C. Seebeck coefficient and power factor of LaCuOSe

The calculated Seebeck coefficients of LaCuOSe are given in Figs. 5(a) and 5(b). Generally, the absolute values of the Seebeck coefficients for both p- and n-type LaCuOSe decrease as the carrier concentration rises. For a specific carrier concentration, the Seebeck coefficient of p-type LaCuOSe along the a axis (S_a solid lines) is larger than that along the c axis (S_c dashed lines) under each temperature [see Fig. 5(a)]. For example, the values of

S_a and S_c at 300 K are 630 and 560 μV/K, respectively, for a doping concentration of 1×10^{18} cm^{-3} (see Table III). On the other hand, n-type LaCuOSe also shows a similar orientation-dependent trend at low electron concentrations. For example, at a temperature of 300 K, the absolute value of the Seebeck coefficient along the a axis ($|S_a|$) is greater than that along the c axis ($|S_c|$; see Table III). However, for n-type LaCuOSe there is a critical carrier-concentration threshold (9×10^{20} cm^{-3}), where $|S_c|$ becomes greater than $|S_a|$ [Fig. 5(b)]. A similar crossover of orientation-dependent Seebeck coefficients is also observed at higher temperatures (i.e., 600 and 900 K) in n-type LaCuOSe. These results demonstrate that the Seebeck coefficients of both p- and n-type LaCuOSe are anisotropic, and the anisotropic Seebeck coefficient for n-type LaCuOSe is affected by carrier concentration. To explore the origin of Seebeck coefficient anisotropy and its carrier-concentration dependence for two systems, the internal relationship between coefficient S and the

electronic structure is further investigated. Generally, the Seebeck coefficient can be described as [71]

$$S = \frac{8\pi^2 k_B^2}{3eh^2} m^* T \left(\frac{\pi}{3n}\right)^{2/3}, \qquad (3)$$

in which T and e are temperature and electronic charge, respectively. Table II shows that, for the p-type system, the hole effective mass along the a axis (2.47 m_e) is much larger than that along the c axis (1.84 m_e), resulting in S_a always being larger than S_c, regardless of temperature and carrier concentration, as observed in Fig. 5(a). In contrast, for the n-type system, electron effective masses along different directions are close to each other, i.e., 0.34 m_e for the a axis and 0.37 m_e for the c axis, due to comparable band curvatures for the bottom of the conduction bands along in-plane and out-of-plane directions [Fig. 1(c)]. Therefore, according to Eq. (3), the values of $|S_a|$ and $|S_c|$ for n-type LaCuOSe are expected to be comparable; however, the results in Fig. 5(b) show clear anisotropy of the Seebeck coefficient in n-type LaCuOSe. This apparent inconsistency can be ascribed to the band-degeneracy-related Seebeck contribution. From the band structure in Fig. 1(c), it is seen that the lowest two conduction bands of LaCuOSe show degenerate behavior, i.e., the energy difference between the lowest two conduction bands at the G point is very small, in the order of 0.1 eV (please refer to previous discussion in Sec. III B). Therefore, for n-type LaCuOSe, the doped electrons will occupy both CBM and CB1, and thus, both will contribute to the Seebeck coefficient [10,18,19]. As a result, the macroscopic Seebeck coefficient, as reflected by Eq. (3), will not only be determined by band curvatures and electron density at the CBM, but also by the degree of conduction-band degeneracy and electron filling on the CB1. Since the degree of band degeneracy for CBM and CB1 is affected by both crystal orientation and overall doping level, it is reasonable to expect different carrier-concentration dependences of $|S_a|$ and $|S_c|$ for n-type LaCuOSe, i.e., crossover at high carrier concentrations, as shown in Fig. 5(b). These phenomena, i.e., the energy-band degeneracy leading to crossover of the Seebeck coefficient in different directions as the carrier concentration rises, are found in many TE materials, such as GeAs$_2$ and GeSe [29,67].

The thermoelectric power factor ($PF = S^2\sigma$) determines the coupling effects between the Seebeck coefficient and electrical conductivity. The calculated PF values of LaCuOSe as a function of carrier concentration are plotted in Figs. 5(c) and 5(d). It is clearly seen that n-type LaCuOSe possesses a significantly higher optimal PF value than that of the p-type system. For instance, the maximum PF value for n-type LaCuOSe (300 K, a axis) is 2.68 mW/mK^2, which is one order of magnitude larger than the value of 0.17 mW/mK^2 for p-type LaCuOSe under the same conditions (300 K, a axis). Interestingly, the obtained highest

PF value of 2.68 mW/mK^2 for LaCuOSe is much larger than those of well-known oxyselenide TE materials, e.g., BiCuOSe [64] and Bi$_2$O$_2$Se [71], for which the maximum PF values are reported to be about 0.18 and 0.95 mW/mK^2 at 300 K, respectively. Similar to σ and S, PF also shows a strong dependence on crystal orientation. The PF values of p- and n-type LaCuOSe along the a axis (solid lines) are much larger than those along the c axis (dashed lines) at the same temperature. For example, at 300 K, the maximum PF value of 2.68 mW/mK^2 for n-type LaCuOSe along the a axis is larger than that of 1.38 mW/mK^2 along the c axis. Furthermore, although p-type LaCuOSe shows a smaller PF, it exhibits more significant anisotropy than that of n-type LaCuOSe. For example, the PF anisotropy (ratio of PF maximum along the a axis to that along the c axis) for n-type LaCuOSe varies from 1.9 to 1.6 as the temperature rises from 300 to 900 K, while the value for p-type LaCuOSe is remarkably larger, i.e., more than 8.7 in the same temperature range. This PF anisotropy behavior results from the synergetic effect of the anisotropic Seebeck coefficient and electrical conductivity.

D. Thermal transport properties of LaCuOSe

Thermal conductivity, κ, includes electronic thermal conductivity, κ_e, and lattice thermal conductivity, κ_l. The electronic thermal conductivity obtained directly from the BoltzTraP2 code, i.e., κ_0, is calculated under closed-circuit conditions. Since the electronic thermal conductivity is defined as the heat current per unit of temperature gradient under open-circuit conditions, the electronic thermal conductivity obtained directly from the BoltzTraP2 code has to be corrected by $\kappa_e = \kappa_0 - T\sigma S^2$ [72]. In this study, the electronic thermal conductivity under open-circuit conditions is obtained by the Wiedemann–Franz law [73,74], i.e., $\kappa_e = L\sigma T$, where L is Lorenz constant. We also compare the electronic thermal conductivities obtained by the BoltzTraP2 code (plus correction) with the values obtained by the Wiedemann-Franz law, and we find that the results obtained by the two different methods are generally consistent with each other. The calculated electronic thermal conductivity as a function of carrier concentration is plotted in Figs. 6(a) and 6(b). Because κ_e and σ are linearly correlated, the variation of κ_e with carrier concentration follows the same trend of σ as that shown in Figs. 4(c) and 4(d). On the other hand, based on the second- and third-order interatomic force constants, the lattice thermal conductivity, κ_l, of LaCuOSe is obtained. Figure 6(c) presents the calculated temperature-dependent κ_l for LaCuOSe with different orientations along with the average value. Since phonon scattering becomes stronger with the increase of temperature, κ_l decreases as the temperature rises. It is noted that the lattice thermal conductivity along the a axis decreases more remarkably than that along

TABLE IV. The lattice thermal conductivities (in W/mK) at room temperature and optimal *ZT* values for LaCuOSe and other TE materials.

		κ_{lav}	κ_{la}	κ_{lb}	κ_{lc}	*ZT* value
LaCuOSe	Our calc	1.73	2.51	2.51	**0.18**	2.71 (900 K)
	Expt. [43]	2.10	–	–	–	–
AgCrSe$_2$	Expt. [85]	~1.6	–	–	–	0.90 (750 K)
AgSbTe$_2$	Expt. [79]	0.68	–	–	–	1.30 (720 K)
BiSbTe	Expt. [86]	~0.9	–	–	–	1.05 (323 K)
BiCuOSe	Other calc [77,82]	0.87	1.10	1.10	**0.41**	0.92 (900 K)
	Expt. [87]	0.77	–	–	–	0.31 (650 K)
Bi$_2$O$_2$Se	Other calc [78]	1.14	1.32	1.32	**0.82**	0.53 (500 K)
	Expt. [88]	1.10	–	–	–	0.15 (800 K)
GeAs$_2$	Other calc [29]	7.31	2.34	18.2	**1.41**	2.78 (800 K)
In$_3$Se$_{3-\delta}$	Expt. [89]	1.18	–	–	–	1.48 (705 K)
PbTe	Other calc [75]	~2.4	–	–	–	–
	Expt. [90]	1.50	–	–	–	0.48 (723 K)
MgAgSb	Expt. [91]	~1.1	–	–	–	0.90 (450 K)
SnSe	Expt. [25]	0.61	0.47	0.69	**0.67**	2.62 (923 K)
SnSe$_2$	Other calc [69]	0.51	0.55	0.55	**0.42**	0.86 (800 K)

the *c* axis. In the temperature range of 300–900 K, the lattice thermal conductivities along the *a* axis (κ_{la}) and *c* axis (κ_{lc}) are calculated to be 2.51–0.84 and 0.18–0.06 W/mK, respectively. The lattice thermal conductivity of LaCuOSe shows strong anisotropic character. The room-temperature κ_{la}/κ_{lc} ratio of 13.64 for LaCuOSe is much larger than that of other anisotropic TE materials, e.g., 6.55 for GeAs$_2$ [29] and 3.44 for phosphorene [33]. Additionally, LaCuOSe exhibits ultralow average lattice thermal conductivity. The average lattice thermal conductivity of 1.73 W/mK is obtained at 300 K, which is consistent with the experimental value of 2.1 W/mK reported by Yasukawa *et al.* [43]. Such a low lattice thermal conductivity of LaCuOSe is comparable to that of well-known TE materials, such as PbTe [75] and Bi$_2$Se$_3$ [76], for which the average lattice thermal conductivities are reported to be about 2.4 and 2.0 W/mK at 300 K, respectively. The lattice thermal conductivities of some typical TE materials are also given in Table IV, and the out-of-plane lattice thermal conductivities are marked in bold type. It is noted that the lattice thermal conductivity for LaCuOSe along the *c* axis has the lowest value among the reported TE materials.

The phonon spectrum and phonon density of state distribution for LaCuOSe are shown in Figs. 6(d) and 6(e). The frequency gap between the high- and low-frequency modes of the optical branches is 2.01 THz. The acoustic branches and low-frequency optical branches are dominated by La, Se, and Cu atoms, and the high-frequency optical modes are dominated by O atoms. Such distributions mainly result from the large mass differences between O and La (Cu, Se) atoms. Generally, the band gap of the phonon spectrum includes the acoustic-optical band gap and the optical-optical band gap. The appearance of the

acoustic-optical band gap can greatly reduce the scattering of acoustic phonons and optical phonons, and thus, increase the lattice thermal conductivity. In other words, the strong coupling between the acoustic branches and optical branches can significantly reduce the lattice thermal conductivity. As for the optical-optical band gap (i.e., the separation of partial density of states between different atoms appearing in the vibration range of the optical phonon), it can cause a slight increase in the lattice thermal conductivity, which is negligible compared with the effect of the acoustic-optical band gap or acoustic-optical coupling [77]. As observed from Fig. 6(e), obvious density of states overlapping occurs in LaCuOSe near a frequency of about 1.5 THz, which indicates that coupling between the acoustic branches and optical branches is strong. This strong coupling reflects large anharmonic scattering, which results in low mean free paths of phonons and suppressed phonon transport, and thus, eventually leads to a low lattice thermal conductivity of LaCuOSe [78]. Similar phenomena are also found in many layered materials, such as Bi$_2$O$_2$Se and Bi$_2$O$_2$Te, for which the lattice thermal conductivities are reported to be 1.14 and 0.58 W/mK at room temperature, respectively [78]. The low lattice thermal conductivity can also be explained by the Grüneisen parameter, γ, which reflects the change of phonon frequency with the crystal volume [25]. High γ means a large lattice anharmonicity, and thus, low κ_l. For example, the average values of γ of SnSe [25], AgSbTe$_2$ [79], and PbTe [75] are 2.87, 2.05, and 1.45, respectively, corresponding to average κ_l values of 0.61, 0.68, and 2.4 W/mK at room temperature. In our calculation, the average γ of 2.67 reflects large lattice anharmonicity in layered LaCuOSe. Thus, this material exhibits a low lattice thermal conductivity.

TABLE V. The calculated phonon velocity, V_g, and Debye temperature, Θ_D, for out-of-plane acoustic branches (ZA), transverse acoustic branches (TA), and longitudinal acoustic branches (LA) for LaCuOSe.

	V_g (km/s)			Θ_D (K)		
	ZA	TA	LA	ZA	TA	LA
G-X (a axis)	4.05	5.00	8.24	10.68	11.15	14.66
G-Z (c axis)	3.38	3.38	6.14	5.24	5.24	9.89

Next, we explore the mechanism for the large anisotropy of lattice thermal conductivity. Generally, the lattice thermal conductivity along the β direction, $\kappa_{l\beta}$ ($\beta = a, c$), can be described as the sum of contributions over all phonon modes, $\lambda(\mathbf{q}, j)$, with the wave vector, $\mathbf{q}$, and branch index, j [29]:

$$\kappa_{l\beta} = \frac{1}{N_{\mathbf{q}}V} \sum \lambda(\mathbf{q},j) C_{\lambda(\mathbf{q},j)} V^2_{\lambda(\mathbf{q},j)} \tau_{\lambda(\mathbf{q},j)}, \qquad (4)$$

in which the $N\mathbf{q}$ and V are the number of sampled $\mathbf{q}$ points in the Brillouin zone and volume of the unit cell, respectively. $C_{\lambda(\mathbf{q},j)}$, $V_{\lambda(\mathbf{q},j)}$, and $\tau_{\lambda(\mathbf{q},j)}$ are the specific heat contribution, phonon group velocity, and phonon relaxation time of every phonon mode, respectively. The lattice heat conduction can be regarded as the diffusion motion of phonons. Therefore, the difference of phonon group velocities (sound velocities) in different directions reflects the anisotropy of lattice thermal conductivity. On the other hand, the large anisotropy for lattice thermal conductivity can also be understood from the internal relationship between the lattice thermal conductivity and Debye temperature, which can be given by the Slack equation [44]:

$$\kappa_{l\beta} = A \frac{\bar{M} \Theta_{D\beta}^3 \delta N^{1/3}}{\gamma^2 T}, \qquad (5)$$

where $\bar{M}$, $\Theta_{D\beta}$, δ, and N are the average mass of the atoms, the Debye temperature along the β direction, lattice size, and number of atoms in the cell, respectively. Generally, the Debye temperature increases with the bonding stiffness; therefore, layered crystals with strong in-plane bonding and weak out-of-plane bonding often show larger Θ_D along the a direction than that along the c direction, and thus, yield a larger in-plane lattice thermal conductivity [80]. The phonon group velocities and Debye temperatures for the out-of-plane acoustic branch (ZA), the transverse acoustic branch (TA), and the longitudinal acoustic branch (LA) are calculated, and the results are presented in Table V. It is found that the phonon group velocities and Debye temperatures along the G-X direction are always much larger than those along the G-Z direction for a specific branch. Hence, according to Eqs. (4) and (5), the lattice thermal conductivity along the a axis direction is much higher than that along the c axis direction under each considered temperature. Similar phenomena are observed for many well-known anisotropic materials [29,78].

E. Figure of merit

With all transport properties available, the figure of merit, ZT, of LaCuOSe can be determined. The results are shown in Figs. 7(a) and 7(b). The ZT values of both p- and n-type LaCuOSe are dependent on the thermal-electric transport directions, while the anisotropy of ZT values is not as obvious as those of PF values and thermal conductivities. Under each considered temperature, the optimal ZT value of n-type LaCuOSe is superior to that of the p-type system, due to relatively large electrical conductivity of the n-type doping system [see Figs. 4(c) and 4(d)]. The maximum ZT values of n- and p-type LaCuOSe are 2.71 and 0.29 for carrier concentrations of about 1.2×10^{20} and 7.1×10^{20} cm^{-3} at 900 K, respectively. The obtained high ZT (2.71), particularly for n-type LaCuOSe, is ascribed to
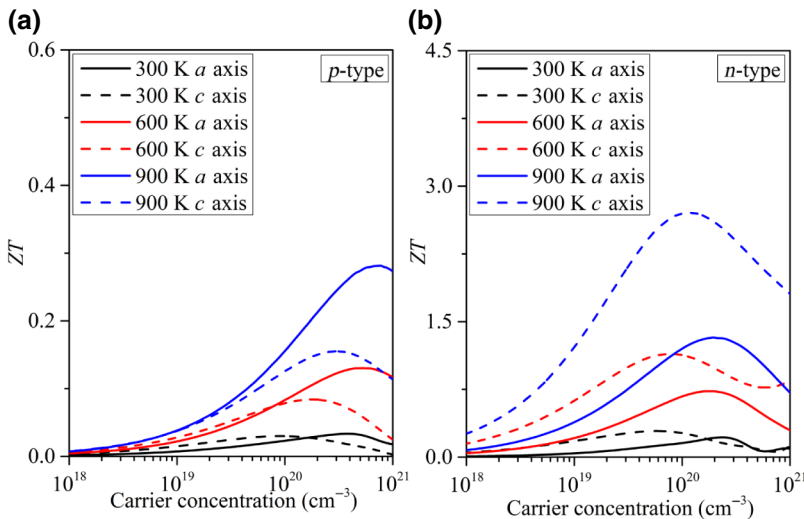

FIG. 7. Calculated figure of merit, ZT, for p- (a) and n-type (b) LaCuOSe as a function of carrier concentration.

the increased electrical conductivity and power factor, as well as suppressed lattice thermal conductivity along the *c* axis. Such a high *ZT* value of *n*-type LaCuOSe is comparable to that of typical anisotropic TE materials, such as SnSe and GeAs$_2$, for which the *ZT* values are reported to be 2.6 at 923 K [25] and 2.78 at 800 K [29], respectively (see Table IV for a more detailed comparison with other TE materials). These results indicate that layered LaCuOSe is a promising TE material, and *n*-type doping is an effective way to improve the TE performance of LaCuOSe.

IV. CONCLUSIONS

The thermoelectric properties of layered oxyselenide LaCuOSe are systematically investigated by first-principles calculations. The electronic and thermal transport coefficients of LaCuOSe exhibit large anisotropy between the in-plane and the out-of-plane directions. A large power factor of 2.10 (1.31) mW/mK^2 along the *a* axis (*c* axis) direction can be achieved at 900 K, because of the large electrical conductivity. Phonon structure calculations suggest strong coupling between acoustic branches and optical branches, which significantly suppresses the bulk thermal transport, leading to low lattice thermal conductivities of 0.84 (0.06) W/mK along the *a* axis (*c* axis) at 900 K. The observed larger power factor and ultralow intrinsic lattice conductivity yield unexpected large *ZT* values of 2.71 (1.32) along the *c* axis (*a* axis) for electron doping at 900 K, and thus, demonstrate that LaCuOSe is a promising material for TE applications. This study also provides an effective route to maximize the TE performance of layered LaCuOSe and has implications in promoting related experimental investigations.

[1] J. T. Gan, J. X. He, R. L. Z. Hoye, A. Mavlonov, F. Raziq, J. L. MacManus-Driscoll, X. Q. Wu, S. Li, X. T. Zu, Y. Q. Zhan, X. Y. Zhang, and L. Qiao, Alpha-CsPbI$_3$ colloidal quantum dots: Synthesis, photodynamics and photovoltaic applications, ACS Energy Lett. **4,** 1308 (2019).

[2] F. Raziq, M. Humayun, A. Ali, T. Wang, A. Khan, Q. Fu, W. Luo, H. Zeng, Z. Zheng, B. Khan, H. Shen, X. Zu, S. Li, and L. Qiao, Synthesis of S-doped porous g-C$_3$N$_4$ by using ionic liquids and subsequently coupled with Au-TiO$_2$ for exceptional cocatalyst-free visible-light catalytic activities, Appl. Catal., B **237,** 1082 (2018).

[3] C. Cai, S. Han, W. Liu, K. Sun, L. Qiao, S. Li, and X. Zu, Tuning catalytic performance by controlling reconstruction process in operan do condition, Appl. Catal., B **260,** 118103 (2019).

[4] X. Q. Wu, *et al.*, Binary Pd/amorphous-SrRuO$_3$ hybrid film for high stability and fast activity recovery ethanol oxidation electrocatalysis, Nano Energy **67,** 104247 (2020).

[5] N. Tian, Z. Y. Zhou, S. G. Sun, Y. Ding, and Z. L. Wang, Synthesis of tetrahexahedral platinum nanocrystals with high-index facets and high electro-oxidation activity, Science **316,** 732 (2007).

[6] L. Chen, L. Lu, H. Zhu, Y. Chen, Y. Huang, Y. Li, and L. Wang, Improved ethanol electrooxidation performance by shortening Pd-Ni active site distance in Pd-Ni-P nanocatalysts, Nat. Commun. **8,** 114136 (2017).

[7] M. S. Dresselhaus, G. Chen, M. Y. Tang, R. G. Yang, and P. Gogna, New directions for low-dimensional thermoelectric materials, Adv. Mater. **19,** 1043 (2010).

[8] Y. Ding, B. Xiao, G. Tang, and J. Hong, Transport properties and high thermopower of SnSe$_2$: A full *ab-initio* investigation, J. Phys. Chem. C **121,** 225 (2017).

[9] N. Wang, M. L. Li, H. Y. Xiao, H. F. Gong, Z. J. Liu, X. T. Zu, and L. Qiao, Optimizing the thermoelectric transport properties of Bi$_2$O$_2$Se monolayer via biaxial strain, Phys. Chem. Chem. Phys. **21,** 15097 (2019).

[10] M. L. Li, N. Wang, M. Jiang, H. Y. Xiao, H. B. Zhang, Z. J. Liu, X. T. Zu, and L. Qiao, Improved thermoelectric performance of bilayer Bi$_2$O$_2$Se by the band convergence approach, J. Mater. Chem. C **7,** 11029 (2019).

[11] T. Ouyang, E. Jiang, C. Tang, J. Li, and J. Zhong, Thermal and thermoelectric properties of monolayer indium triphosphide (InP$_3$): A first-principles study, J. Mater. Chem. A **6,** 21532 (2018).

[12] G. J. Snyder and E. S. Toberer, Complex thermoelectric materials, Nat. Mater. **7,** 105 (2008).

[13] G. Li, G. Ding, and G. Gao, Thermoelectric properties of SnSe2 monolayer, J. Phys. Condens. Matter **29,** 015001 (2017).

[14] B. Kanishka, H. Jiaqing, I. D. Blum, W. Chun-I, T. P. Hogan, D. N. Seidman, V. P. Dravid, and M. G. Kanatzidis, High-performance bulk thermoelectrics with all-scale hierarchical architectures, Nature **489,** 414 (2012).

[15] X. Meng, Z. Liu, C. Bo, D. Qin, H. Geng, C. Wei, L. Fu, J. He, Z. Ren, and J. Sui, Grain boundary engineering for achieving high thermoelectric performance in n-type skutterudites, Adv. Energy Mater. **7,** 1602582 (2017).

[16] D. Ding, D. Wang, M. Zhao, J. Lv, H. Jiang, C. Lu, and Z. Tang, Interface engineering in solution-processed nanocrystal thin films for improved thermoelectric performance, Adv. Mater. **29,** 1603444 (2017).

[17] V. T. Tran, J. S. Martin, and P. Dollfus, High thermoelectric performance in graphene nanoribbons by graphene/BN interface engineering, Nanotechnology **26,** 495202 (2015).

[18] Y. Pei, H. Wang, and G. J. Snyder, Band engineering of thermoelectric materials, Adv. Mater. **24,** 6125 (2012).

[19] Z. Hong, W. Sun, R. Armiento, P. Lazic, and G. Ceder, Band structure engineering through orbital interaction for enhanced thermoelectric power factor, Appl. Phys. Lett. **104,** 1457 (2014).

[20] Y. Lei, Z. G. Chen, G. Han, H. Min, Y. Zou, and Z. Jin, High-performance thermoelectric Cu_2Se nanoplates through nanostructure engineering, Nano Energy **16,** 367 (2015).

[21] J. Zhang, D. Wu, D. He, D. Feng, M. Yin, X. Qin, and J. He, Extraordinary thermoelectric performance realized in n-type pbte through multiphase nanostructure engineering, Adv. Mater. **29,** 1703148 (2017).

[22] C. X. Yu, G. Zhang, Y. W. Zhang, and L. M. Peng, Strain engineering on the thermal conductivity and heat flux of thermoelectric Bi_2Te_3 nanofilm, Nano Energy **17,** 104 (2015).

[23] H. Y. Lv, Enhanced thermoelectric performance of phosphorene by strain-induced band convergence, Phys. Rev. B **90,** 085433 (2014).

[24] S. D. N. Luu and P. Vaqueiro, Synthesis, characterisation and thermoelectric properties of the oxytelluride Bi_2O_2Te, J. Solid State Chem. **226,** 219 (2015).

[25] L. D. Zhao, S. H. Lo, Y. Zhang, H. Sun, G. Tan, C. Uher, C. Wolverton, V. P. Dravid, and M. G. Kanatzidis, Ultralow thermal conductivity and high thermoelectric figure of merit in SnSe crystals, Nature **508,** 373 (2014).

[26] Y. Tang, Z. M. Gibbs, L. A. Agapito, G. Li, H. S. Kim, M. B. Nardelli, S. Curtarolo, and G. J. Snyder, Convergence of multi-valley bands as the electronic origin of high thermoelectric performance in $CoSb_3$ skutterudites, Nat. Mater. **14,** 1223 (2015).

[27] B. Li, H. Wang, Y. Kawakita, Q. Zhang, M. Feygenson, H. L. Yu, D. Wu, K. Ohara, T. Kikuchi, K. Shibata, T. Yamada, X. K. Ning, Y. Chen, J. Q. He, D. Vaknin, R. Q. Wu, K. Nakajima, and M. G. Kanatzidis, Liquid-like thermal conduction in intercalated layered crystalline solids, Natature Mater. **17,** 226 (2018).

[28] M. D. Nielsen, V. Ozolins, and J. P. Heremans, Lone pair electrons minimize lattice thermal conductivity, Energy Environ. Sci. **6,** 570 (2013).

[29] F. Q. Wang, Y. Guo, Q. Wang, Y. Kawazoe, and P. Jena, Exceptional thermoelectric properties of layered $GeAs_2$, Chem. Mater. **29,** 9300 (2017).

[30] B. R. Ortiz, J. M. Adamczyk, K. Gordiz, T. Braden, and E. S. Toberer, Towards the high-throughput synthesis of bulk materials: Thermoelectric PbTe-PbSe-SnTe-SnSe alloys, Mol. Syst. Des. Eng. **4,** 407 (2019).

[31] W. Chen, J. H. Pohls, G. Hautier, D. Broberg, S. Bajaj, U. Aydemir, Z. M. Gibbs, H. Zhu, M. Asta, G. J. Snyder, B. Meredig, M. A. White, K. Persson, and A. Jain, Understanding thermoelectric properties from high-throughput calculations: Trends, insights, and comparisons with experiment, J. Mater. Chem. C **4,** 4414 (2016).

[32] R. Li, X. Li, L. Xi, J. Yang, D. J. Singh, and W. Zhang, High-throughput screening for advanced thermoelectric materials: Diamond-like ABX_2 compounds, ACS Appl. Mater. Interfaces **11,** 24859 (2019).

[33] L. Zhu, G. Zhang, and B. Li, Coexistence of size-dependent and size-independent thermal conductivities in phosphorene, Phys. Rev. B **90,** 214302 (2014).

[34] J. Qiao, X. Kong, Z. X. Hu, F. Yang, and W. Ji, High-mobility transport anisotropy and linear dichroism in few-layer black phosphorus, Nat. Commun. **5,** 4475 (2014).

[35] Y. Zhao, J. Qiao, P. Yu, Z. Hu, Z. Lin, S. P. Lau, Z. Liu, W. Ji, and Y. Chai, Extraordinarily strong interlayer interaction in 2D layered PtS_2, Adv. Mater. **28,** 2399 (2016).

[36] Y. Zhao, J. Qiao, Z. Yu, P. Yu, K. Xu, S. P. Lau, W. Zhou, Z. Liu, X. Wang, and W. Ji, High-electron-mobility and air-stable 2D layered $PtSe_2$ FETs, Adv. Mater. **29,** 1604230 (2017).

[37] H. Hiramatsu, K. Ueda, H. Ohta, T. Kamiya, M. Hirano, and H. Hosono, Excitonic blue luminescence from p-$LaCuOSe$/n-$InGaZn_5O_8$ light-emitting diode at room temperature, Appl. Phys. Lett. **87,** L604 (2005).

[38] H. Yanagi, S. Ohno, T. Kamiya, H. Hiramatsu, M. Hirano, and H. Hosono, Magnetic and carrier transport properties of Mn-doped p-type semiconductor LaCuOSe: An investigation of the origin of ferromagnetism, J. Appl. Phys. **100,** 33717 (2006).

[39] H. Hidenori, K. Toshio, T. Tetsuya, I. Eiji, M. Teruyasu, I. Yuichi, K. Keisuke, and H. Hideo, Origins of hole doping and relevant optoelectronic properties of wide gap p-type semiconductor, LaCuOSe, J. Am. Chem. Soc. **132,** 15060 (2010).

[40] F. E. Akkad, B. Mansour, and T. Hendeya, Electrical and thermoelectric properties of Cu_2Se and Cu_2S, Mater. Res. Bull. **16,** 535 (1981).

[41] R. Venkatasubramanian, E. Siivola, T. Colpitts, and B. O'Quinn, Thin-film thermoelectric devices with high room temperature figures of merit, Nature **413,** 597 (2001).

[42] H. Hiramatsu, K. Ueda, H. Ohta, M. Hirano, T. Kamiya, and H. Hosono, Wide gap p-type degenerate semiconductor: Mg-doped LaCuOSe, Thin Solid Films **445,** 304 (2003).

[43] M. Yasukawa, K. Ueda, and H. Hosono, Thermoelectric properties of layered oxyselenides $La_{1-x}Sr_xCuOSe$ (x=0 to 0.2), J. Appl. Phys. **95,** 3594 (2004).

[44] S. K. Saha and G. Dutta, Elastic and thermal properties of the layered thermoelectrics BiOCuSe and LaOCuSe, Phys. Rev. B **94,** 125209 (2016).

[45] G. Kresse and J. Furthmuller, Efficiency of *ab-initio* total energy calculations for metals and semiconductors using a plane-wave basis set, Comput. Mater. Sci. **6,** 15 (1996).

[46] G. Kresse and J. Furthmuller, Efficient iterative schemes for ab initio total-energy calculations using a plane-wave basis set, Phys. Rev. B **54,** 11169 (1996).

[47] G. Kresse and J. Hafner, Ab-initio molecular-dynamics for liquid-metals, Phys. Rev. B **47,** 558 (1993).

[48] J. P. Perdew, K. Burke, and M. Ernzerhof, Generalized Gradient Approximation Made Simple, Phys. Rev. Lett. **77,** 3865 (1996).

[49] S. Zhang, H. Y. Xiao, S. M. Peng, G. X. Yang, Z. J. Liu, X. T. Zu, S. Li, D. J. Singh, L. W. Martin, and L. Qiao, Band-Gap Reduction in $(BiCrO_3)(m)/(BiFeO_3)(n)$ Superlattices: Designing Low-Band-Gap Ferroelectrics, Phys. Rev. Appl. **10,** 044004 (2018).

[50] L. Qiao, S. Zhang, H. Y. Xiao, D. J. Singh, K. H. L. Zhang, Z. J. Liu, X. T. Zu, and S. Li, Orbital controlled band gap engineering of tetragonal $BiFeO_3$ for optoelectronic applications, J. Mater. Chem. C **6,** 1239 (2018).

[51] J. Heyd, G. E. Scuseria, and M. Ernzerhof, Hybrid functionals based on a screened Coulomb potential, J. Chem. Phys. **118,** 8207 (2003).

[52] G. K. H. Madsen, J. Carrete, and M. J. Verstraete, Boltztrap2, a program for interpolating band structures and calculating semi-classical transport coefficients, Comput. Phys. Commun. **231,** 140 (2018).

[53] J. Bardeen and W. S. Shockley, Deformation potentials and mobilities in non-polar crystals, Phys. Rev. **80,** 72 (1950).

[54] A. Togo and I. Tanaka, First principles phonon calculations in materials science, Scr. Mater. **108,** 1 (2015).

[55] L. Wu, J. Carrete, N. A. Katcho, and N. Mingo, ShengBTE: A solver of the boltzmann transport equation for phonons, Comput. Phys. Commun. **185,** 1747 (2014).

[56] K. Momma and F. Izumi, VESTA: A three-dimensional visualization system for electronic and structural analysis, J. Appl. Crystallogr. **41,** 653 (2008).

[57] Y. Ohki, S. Komatsuzaki, Y. Takahashi, K. Takase, Y. Takano, and K. Sekizawa, New and Old concepts in thermoelectric materials, Am. Inst. Phys. **850,** 1309 (2006).

[58] V. Vulchev, L. Vassilev, S. Harizanova, M. Khristov, E. Zhecheva, and R. Stoyanova, Improving of the thermoelectric efficiency of $LaCoO_3$ by double substitution with nickel and iron, J. Phys. Chem. C **116,** 13507 (2012).

[59] L. Qiao, J. H. Jang, D. J. Singh, Z. Gai, H. Xiao, A. Mehta, R. K. Vasudevan, A. Tselev, Z. Feng, H. Zhou, S. Li, W. Prellier, X. Zu, Z. Liu, A. Borisevich, A. P. Baddorf, and M. D. Biegalski, Dimensionality controlled octahedral symmetry-mismatch and functionalities in epitaxial $LaCoO_3/SrTiO_3$ heterostructures, Nano Lett. **15,** 4677 (2015).

[60] L. Qiao, T. C. Droubay, T. Varga, M. E. Bowden, V. Shutthanandan, Z. Zhu, T. C. Kaspar, and S. A, Chambers, epitaxial growth, structure, and intermixing at the $LaAlO_3/SrTiO_3$ interface as the film stoichiometry is varied, Phys. Rev. B **83,** 085408 (2011).

[61] L. Qiao, K. H. L. Zhang, M. E. Bowden, T. Varga, V. Shutthanandan, R. Colby, Y. Du, B. Kabius, P. V. Sushko, M. D. Biegalski, and S. A. Chambers, The impacts of cation stoichiometry and substrate surface quality on nucleation, structure, defect formation and intermixing in complex oxide heteroepitaxy-$LaCrO_3$ on $SrTiO_3(001)$, Adv. Funct. Mater. **23,** 2953 (2013).

[62] B. W. Rudyk, P. E. R. Blanchard, R. G. Cavell, and A. Mar, X-ray photoelectron and absorption spectroscopy of mixed lanthanum copper oxychalcogenides $LaCuOSe_{1-x}Te_x$ ($0 \le x \le 1$), J. Alloys Compd. **514,** 199 (2012).

[63] N. D. Zhang and H. Gong, P-type transparent LaCuOS semiconductor synthesized via a novel two-step solid state reaction and sulfurization process, Ceram. Int. **43,** 6295 (2017).

[64] L. D. Zhao, J. He, D. Berardan, Y. Lin, J. F. Li, C. W. Nan, and N. Dragoe, Bicuseo oxyselenides: New promising thermoelectric materials, Energy Environ. Sci. **7,** 2900 (2014).

[65] S. Nosé, A unied formulation of the constant temperature molecular dynamics methods, J. Chem. Phys. **81,** 511 (1984).

[66] M. Cutler, J. Leavy, and R. Fitzpatrick, Electronic transport in semimetallic cerium sulfide, Phys. Rev. **133,** A1143 (1964).

[67] S. Q. Hao, F. Y. Shi, V. P. Dravid, M. G. Kanatzidis, and C. Wolverton, Computational prediction of high thermoelectric performance in hole doped layered GeSe, Chem. Mater. **28,** 3218 (2016).

[68] K. Kutorasinski, B. Wiendlocha, S. Kaprzyk, and J. Tobola, Electronic structure and thermoelectric properties of n- and p-type SnSe from first-principles calculations, Phys. Rev. B **91,** 205201 (2015).

[69] B. Z. Sun, Z. Ma, C. He, and W. Kechen, Anisotropic thermoelectric properties of layered compounds in SnX_2 ($X = S$, Se): A promising thermoelectric, Phys. Chem. Chem. Phys. **17,** 29844 (2015).

[70] J. Yang, G. Yang, G. Zhang, and Y. X. Wang, Low effective mass leading to an improved ZT value by 32% for n-type BiCuSeO: A first-principles study, J. Mater. Chem. A **2,** 13923 (2014).

[71] D. Guo, C. Hu, Y. Xi, and K. Zhang, Strain effects to optimize thermoelectric properties of doped Bi_2O_2Se via TranBlaha modified Becke-Johnson density functional theory, J. Phys. Chem. C **117,** 21597 (2013).

[72] G. K. H. Madsen and D. J. Singh, Boltztrap. A code for calculating band-structure dependent quantities, Comput. Phys. Commun. **175,** 67 (2006).

[73] M. Jonson and G. D. Mahan, Mott's formula for the thermopower and the Wiedemann-Franz law, Phys. Rev. B: Condens. Matter **21,** 4223 (1980).

[74] N. Stojanovic, D. H. S. Maithripala, J. M. Berg, and M. Holtz, Thermal conductivity in metallic nanostructures at high temperature: Electrons, phonons, and the Wiedemann-Franz law, Phys. Rev. B **82,** 2283 (2010).

[75] G. A. Slack, in *Solid State Physics*, edited by F. Seitz, D. Turnbull, H. Ehrenreich (Solid State Physics, New York, 1979), Vol. 34, pp. 1–71.

[76] J. Navratil, J. Horak, T. Plechacek, S. Kamba, P. Lost'ak, J. S. Dyck, W. Chen, and C. Uher, Conduction band splitting and transport properties of Bi_2Se_3, J. Solid State Chem. **177,** 1704 (2004).

[77] L. Gang, H. Sun, Z. Jian, Q. Li, and X. G. Wan, Thermal properties of layered oxychalcogenides BiCuOCh (Ch=S, Se, and Te): A first-principles calculation, J. Appl. Phys. **119,** 185109 (2016).

[78] C. Wang, G. Ding, X. Wu, S. Wei, and G. Gao, Electron and phonon transport properties of layered Bi_2O_2Se and Bi_2O_2Te from first-principles calculations, New J. Phys. **20,** 123014 (2018).

[79] D. T. Morelli, V. Jovovic, and J. P. Heremans, Intrinsically Minimal Thermal Conductivity in Cubic I-V-VI(2) Semiconductors, Phys. Rev. Lett. **101,** 035901 (2008).

[80] X. Gu, Y. Wei, X. Yin, B. Li, and R. Yang, Phononic thermal properties of two-dimensional materials, Rev. Mod. Phys. **90,** 041002 (2017).

[81] S. Muhammady, I. M. Sutjahja, A. Rusydi, T. Winata, K. Takase, and Y. Darma, Unrevealed electronic and optical properties of the layered oxychalcogenides (LaO)CuCh (Ch=S, Se, Te): A density-functional study, Jpn. J. Appl. Phys. **56,** 121201 (2017).

[82] D. Zou, S. Xie, Y. Liu, J. Lin, and J. Li, Electronic structures and thermoelectric properties of layered BiCuOCh oxychalcogenides (Ch = S, Se and Te): First-principles calculations, J. Mater. Chem. A **1,** 8888 (2013).

[83] H. Hiramatsu, H. Yanagi, T. Kamiya, K. Ueda, M. Hirano, and H. Hosono, Crystal structures, optoelectronic properties, and electronic structures of layered oxychalcogenides MCuOCh (M = Bi, La; Ch = S, Se, Te): Effects of electronic configurations of M^{3+} ions, Chem. Mater. **20,** 326 (2008).

[84] Y. Tang, F. Cheng, D. C. Li, S. P. Deng, Z. Chen, L. Q. Sun, W. T. Liu, L. X. Shen, and S. K. Deng, Contrastive thermoelectric properties of strained SnSe crystals from the first-principles calculations, Phys. B **539,** 8 (2018).

[85] S. Bhattacharya, A. Bohra, R. Basu, R. Bhatt, S. Ahmad, K. N. Meshram, A. K. Debnath, A. Singh, S. K. Sarkar, M. Navneethan, Y. Hayakawa, D. K. Aswal, and S. K. Gupta, High thermoelectric performance of $(AgCrSe_2)_{(0.5)}(CuCrSe_2)_{(0.5)}$ nano-composites having all-scale natural hierarchical architectures, J. Mater. Chem. A **2,** 17122 (2014).

[86] B. Poudel, Q. Hao, Y. Ma, Y. Lan, A. Minnich, B. Yu, X. Yan, D. Wang, A. Muto, D. Vashaee, X. Chen, J. Liu, M. S. Dresselhaus, G. Chen, and Z. Ren, High-thermoelectric performance of nanostructured bismuth antimony telluride bulk alloys, Science **320,** 634 (2008).

[87] H. Y. Zhu, T. C. Su, H. T. Li, C. Y. Pu, D. W. Zhou, P. W. Zhu, and X. Wang, High pressure synthesis, structure and thermoelectric properties of BiCuChO(Ch = S, Se, Te), J. Eur. Ceram. Soc. **37,** 1541 (2017).

[88] P. Ruleova, C. Drasar, P. Lostak, C. P. Li, S. Ballikaya, and C. Uher, Thermoelectric properties of Bi_2O_2Se, Mater. Chem. Phys. **119,** 299 (2010).

[89] J. S. Rhyee, K. H. Lee, S. M. Lee, E. Cho, S. I. Kim, E. Lee, Y. S. Kwon, J. H. Shim, and G. Kotliar, Peierls distortion as a route to high thermoelectric performance in $In_4Se_{3-\delta}$ crystals, Nature **459,** 965 (2009).

[90] Y. Ling and Y. Liu, Electrical and thermal transport properties of Pb-based chalcogenides: PbTe, PbSe, and PbS, J. Alloys Compd **514,** 0 (2012).

[91] H. Zhao, J. Sui, Z. Tang, Y. Lan, Q. Jie, D. Kraemer, K. McEnaney, A. Guloy, G. Chen, and Z. Ren, High thermoelectric performance of MgAgSb-based materials, Nano Energy **7,** 97 (2014).

Correction: The second entry in the first column of Table I contained an error and has been fixed.